

Time-Latitude Distribution of Prominences for 10 Solar Cycles: A study using Kodaikanal, Meudon and Kanzelhohe Data

Subhamoy Chatterjee¹, Manjunath Hegde¹, Dipankar Banerjee^{1,2}, B. Ravindra¹, Scott W. McIntosh³

¹Indian Institute of Astrophysics, Koramangala, Bangalore 560034, India

²Center of Excellence in Space Sciences India, IISER Kolkata, Mohanpur 741246, West Bengal, India

³High Altitude Observatory, National Center for Atmospheric Research, PO Box 3000, Boulder, Colorado 80307, USA

Key Points:

- Calibration of Ca II K disc-blocked digitised images as recorded in Kodaikanal observatory for the period of 1906-2002.
- Automated detection of prominences for 10 solar cycles (1906-2018) from Ca II K disc-blocked digitised images as recorded in Kodaikanal Observatory and H α images from Meudon and Kanzelhohe Observatory.
- Clear identification of pole-ward migration for all the cycles, estimation of migration rates from pole-ward branches near the onset and close to pole through piece-wise linear fits with error bars. Those can act as vital inputs to polar field build-up process.

arXiv:1802.07556v2 [astro-ph.SR] 6 May 2020

Abstract

Solar prominences are structures of importance because of their role in polar field reversal. We study the long-term variation of the time latitude distribution of solar prominences in this article. To accomplish this, we primarily used the digitised disc-blocked Ca II K spectroheliograms as recorded from Kodaikanal Solar Observatory for the period of 1906 – 2002. For improving the data statistics we included full disc H_{α} images from Meudon and Kanzelhoehe Observatory which are available after 1980. We developed an automated technique to identify the latitudinal locations of prominences in daily images from all three datasets. Derived time-latitude distribution clearly depicted pole-ward migration of prominence structures for 10 cycles (15-24). Unlike previous studies, we separated the rate of pole-ward migration during on-set and near pole, using piece-wise linear fits. In most cases, we found acceleration in pole-ward migration with the change occurring near $\pm 70^{\circ}$ latitudes. The derived migration rates for such large number of solar cycles can provide important inputs towards understanding polar field build-up process.

1 Introduction

Magnetic field is responsible for the heterogeneity as observed on the Sun in different temporal and spatial scales. Continuous monitoring of the solar magnetic field has been possible only in recent past with the launch of space-borne telescopes like Michelson Doppler Imager (MDI, on the Solar Heliospheric Observatory, SoHO, (Hoeksema et al., 1997)) and more recently Helioseismic and Magnetic Imager (HMI, on the Solar Dynamics Observatory, SDO (Fleck et al., 2012)). Before that magnetic field measurements in low resolution was initiated by ground-based observatories like Mount Wilson and most prominently by Wilcox Solar Observatory since the year 1976 (Bogart, Hoeksema, & Scherrer, 1992; “Wilcox Solar Observatory”, 2000) and KittPeak/National Solar Observatory(NSO) since 1970 (Livingston & Harvey, 1971; Minarovjech, Rušin, & Saniga, 2011). These data sources have been extensively used for solar cycle studies (Harvey & Munoz-Jaramillo, 2015). To trace back the solar magnetic field activity before 1976 different proxies have been used. Some of the prominent features serving as proxies are sunspots, plages and filaments/prominences.

Prominences/filaments are structures formed in the solar atmosphere following magnetic polarity inversion lines. They are formed in the chromosphere by cool dense (hundred times cooler and denser than the coronal material) plasma held in place by solar magnetic fields (Engvold, 2015; Gibson, 2018; Martin, 2015). At the limb they appear as bright features when observed in few optical, EUV lines such as H_{α} , Ca II K, He II 304 Å. They appear as dark elongated hairlike features on the disc for example in H_{α} 6562.8 Å or in He II 304 Å (named as filaments). Prominences present themselves in different morphology, lifetime and complexity in magnetic field environments. Orientation of small leg-like structures called ‘barbs’ bifurcating from filaments, known as ‘chirality’, provides important information about the supporting magnetic field morphology. Martens and Zwaan (2001) presented an interesting model on formation and evolution of filaments/prominences of different chiralities through ‘head-tail linkage’ of different bipolar magnetic regions resulting in ‘convergence and cancellation’. Another comprehensive study on filament formation and its hemispheric distribution was made by Mackay (2015). Yeates and Mackay (2009) connected global magnetic field distribution and origin of hemisphere-wise filament chiralities. As a follow-up study, Yeates and Mackay (2012) predicted dependence of high-latitude filament hemispheric chirality patterns on cycle phase using NSO/Kitt Peak cycle 23 magnetograms and emphasized on importance of coronal magnetic field memory. Thus long term study of prominences over several cycles and at different phases of solar cycle can give valuable insight on the physics of the solar atmosphere. There have been several studies to correlate eruptive prominence distributions and coronal mass ejections (CMEs) (Fan, 2015; Gilbert et al., 2000; Gopalswamy, 2015; Gopalswamy et al., 2003; Lugaz, 2015; Schrijver et al., 2008; Webb, 2015). Lockyer (1908, 1922, 1931) using coronal drawings and photographs obtained during the total solar eclipse suggested that there is an intimate connection between the distribution of prominences around the solar limb and the forms of corona. Though prominences form all over the Sun, their latitudinal distribution changes significantly with time being correlated with global properties of large scale magnetic fields on solar surface.

As pointed out earlier, prominences were first seen during total solar eclipses. Early history of prominence observations can be found in Tandberg-Hanssen (1974, 1998). Zone of polar prominences and its pole-ward migration was discovered by Secchi (1872). To probe the change in time-latitude distribution of prominences and its heterogeneity for the understanding and predicting solar magnetic fields over longer time scales (Bhowmik & Nandy, 2018), one needs long-term, homogeneous datasets. Surface flux transport dynamo models have largely been effective in realizing of polar field build-up which remains to be the governing factor in predicting solar cycles (Bhowmik & Nandy, 2018; Muñoz-Jaramillo et al., 2012). It is thus worth understanding the long-term behaviour of polar prominences and their connection to polar magnetic fields. Along with the observations of on-disc filaments with spectroheliograph, systematic prominence observations were also carried out. Daily prominence observation at the Kodaikanal Solar Observatory (KoSO hereafter) started before the observational set-up for H_{α} was ready. This is because of the fact that the prominences were observed in Ca II K at KoSO above the solar limb by blocking the disc. So, full-disc and disc blocked observation started simultaneously at KoSO in Ca II K wavelength using spectroheliograph. Meudon observatory started prominence observation in H_{α} consistently after KoSO since 1919. Lomnický Peak Observatory also recorded solar prominences in H_{α} from 1967 (Bumba, Rusin, & Rybansky, 1990; Minarovjech, Rybansky, & Rusin, 1998a; Rusin et al., 1994; Rušin et al., 1988) until 2009. It is worth mentioning that Kislovodsk solar station in Russia started observing the Sun in H_{α} since 1957 and recorded filaments, prominences in the form of synoptic charts (Makarov et al., 2001; Makarov, Tlatov, & Sivaraman, 2001, 2003). The observatory continues to make this observations till today. Recently, ground based disc-blocked prominence observation in H_{α} has been initiated at Kanzelhöhe Solar Observatory since 2009.

There have been several works reported in past using these historical data on prominences. From such datasets both pole-ward and equator-ward migration were shown by Abetti (1957). Waldmeier (1973) established 3 narrow zones, which show different latitudinal behaviour in the 11-year cycle, namely sunspot prominences, stable long-lived prominences and polar zone prominences forming at latitudes around 45° during minimum and migrating towards poles around solar maximum gaining a velocity of $10 - 25 \text{ ms}^{-1}$. The change of migration rates from lower latitudes to near poles was pointed out by Makarov, Tlatov, and Sivaraman (2001). D’Azambuja and D’Azambuja (1948) made a large number of measurements on filaments and prominences during the period of 1919 – 1930 and found on an average that all prominences have a low pole-ward drift in both the hemispheres. Verma (2000) studied the distribution and asymmetry of Solar Active Prominences (SAP) for the period of 1957 – 1998 (solar cycles 19 – 23) and found that E – W asymmetry of SAP events is not significant. He reported that N – S asymmetry of SAP events is significant and it has no relation with the solar maximum or solar minimum during solar cycles. Another study on asymmetry of SAP spatial distribution was made by Joshi et al. (2009). Liu et al. (2012) using Solar Limb Prominence CATCHer and Tracker (SLIPCAT), studied prominences during the period 2007 – 2009. Shimojo (2013) using Nobeyama Radioheliograph reported the unusual migration of prominences producing region of activities in the southern hemisphere and interpreted the anomalies from the distribution of the photospheric magnetic field during the cycles 23 – 24. Parenti (2014) reviewed characteristic properties of prominences and filaments as derived from observations. Other studies were made to quantify the time-latitude distribution of prominence (Bumba et al., 1990; Minarovjech et al., 1998a) and correlated them with other solar cycle indices (Makarov, Tlatov, & Sivaraman, 2001) for making cycle prediction (Makarov et al., 2003). Long-term study on filaments have also been made using hand-drawn Synoptic maps from Meudon Observatory (Tlatov, Kuzanyan, & Vasil’yeva, 2016) and MacIntosh database (Mazumder, Bhowmik, & Nandy, 2018). These studies provided important results on filament tilt angles, their latitude dependence, rush to the poles and polar reversal.

Most of the aforementioned works focused on temporal variation in spatial distribution of filaments/prominences but are limited to either short time-span or hand-drawn data. Naturally, more reliable results require a uniform digitised long-term dataset in gray-scale. Combined data from different observatories require cross calibration, otherwise detection techniques with same parameters but as applied to different data are not comparable. Rybák et al. (2011) cross-calibrated data from Lomnický Peak Observatory (1967 – 2009) and Kanzelhöhe Solar Observatory (2009 – 2010)

before detection of prominences. In this context, it is worth mentioning that KoSO recorded prominence observations from 1906 until 2002 on daily basis with an instrument of unchanged optics. This ensured uniformity in the KoSO prominence data quality making it advantageous for feature detection. Prominence data from Kodaikanal for the period 1904 – 1914 is discussed by Evershed and Evershed (1917) and by Moss (1946) for the period 1905 – 1928. Half-yearly summaries of prominence observations were published in the Bulletin of the Kodaikanal Observatory. Using this data, prominence eruption was also reported in Evershed (1917). But the notable study from KoSO prominence data was made by Ananthakrishnan (1952). He performed manual identification of prominences during the period 1905 – 1950 and found a relationship between prominence activity and sunspot cycle. General review and discussion about the prominence data collected at Kodaikanal observatory was summarised by Ananthakrishnan (1954). KoSO photographic plates have been recently digitised for the entire duration of observations. In modern times it is important to identify and detect structures such as prominences using computer codes for avoiding human bias and increasing speed. Rybák et al. (2011) have used the digitized Lomnický Peak Observatory and Kanzelhohe Solar Observatory data to detect the prominence structures through semi-automated codes. Later, they have cross-calibrated these two datasets as well.

Our objective is to detect prominence locations from the digitized KoSO data in a fully automated manner. In the present study to improve the statistics and to make the detection up-to-date, we also included the full disc H_{α} data from Meudon (1980-2002) and Kanzelhohe Observatory (2000-2018) by blocking the disc and bringing them to equal footing as KoSO data. In this article we present an automated technique to identify the prominence latitudes from combined (KoSO-Meudon-kanzelhohe) disc-blocked dataset. We describe the data in Section 2 followed by analysis of data in Section 3 encompassing calibration, prominence detection technique and results on poleward migration. We finally discuss the results of the study in Section 4 and conclude in Section 5.

2 Data Description

In following three subsections we describe the three datasets used in our study for prominence detection.

2.1 Kodaikanal Dataset

The Ca II K line is very broad in wavelength coverage with 3 prominent positions namely K_1 , K_2 and K_3 on the line profile. The K_3 region (3933.7Å), is where we see filaments and prominences similar to those seen in H_{α} but with much less contrast and less well defined boundaries. Photographic observations of solar prominences in Ca II K line (central wavelength 3933.7Å, passband 0.5Å) using spectroheliograph were started at Kodaikanal during 1905 (Ananthakrishnan, 1954). The nominal spectral passband remained constant at 0.5Å throughout the study time (Chatterjee, Mandal, & Banerjee, 2017). However, there are studies that predict change of bandwidth and center wavelength for this dataset from change in contrast of the images (Chatzistergos, Ermolli, Krivova, & Solanki, 2019; Chatzistergos, Ermolli, Solanki, et al., 2019). With weather permitting (when the sky and seeing conditions were good), the routine Ca II K observations were made between 02:00 to 04:30 UT at KoSO with the spectroheliograph. This data is available in 8-bit and 16-bit digitised form. The 8-bit version was presented in Ermolli et al. (2009) as the most uniform dataset in terms of resolution, large-scale inhomogeneity and contrast among different available long-term datasets. An accurate photometric calibration of this series was made by Chatzistergos, Ermolli, Solanki, and Krivova (2018) to make the dataset ready for irradiance calculation and also detection of plages (Chatzistergos, Ermolli, Krivova, & Solanki, 2019). Recently, the 16-bit series was studied by Chatzistergos, Ermolli, Solanki, et al. (2019) confirming its superiority over the 8-bit series in terms of uniformity. It is the same instrument which was used to make the disc-blocked Ca II K spectroheliograms as well. In order to get the contrast for the prominences, the chromosphere (disc

Table 1. Datasets used for prominence detection

Observatory	Data Type	Time span
Kodaikanal	Ca II K disc blocked	1906–2002
Meudon	H $_{\alpha}$ full disc	1980–2002 ¹
Kanzelhohe	H $_{\alpha}$ full disc	2000–2018 ²

region) was mechanically blocked by a circular mask of same size before capturing the image on photographic plates/films. The telescope used for this had an optics with a 30 cm objective, with f-ratio of f/21 (Priyal, Singh, Ravindra, Priya, & Amareswari, 2014). This optics was unchanged throughout the observation period ensuring uniformity in quality. The disc blocked images were digitized recently through a 16-bit digitization unit at KoSO consisting of an uniform illumination source, imaging optics for proper magnification and a 4096×4096 CCD cooled at -100°C . The digitized images from 1906 until 2002 (Table 1) used in our study were in all ‘.fits’ format and of size 4096×4096 with a pixel scale of ≈ 0.88 arcsec. Figure 1a shows the typical digitized disc-occulted chromospheric image. The date and time of the observation are written on each of the plate at one corner, on the opposite side of emulsion material. The white line on the right bottom corner is the holder for occulter disc. Double and single dots outside the occulter represent the North and South pole of the Sun respectively. Due to the unavailability of pole marking on the images taken before 1906, we used here the data starting from 1906. Many prominences could be seen in the digitized image on the limb. Figure 2a depicts the number of days of observational data available per year for different years. On an average ≈ 269 observing days are available each year for the analysis before 1975. But, after 1975 the average number of days of available data per year drops to ≈ 143 . Other data sources, as mentioned in Table 1, were used to complement Kodaikanal data in later years and complete the analysis till current solar cycle.

2.2 Meudon Dataset

Digitised full-disc H $_{\alpha}$ spectroheliograms (Figure 1b) from Meudon Observatory (Demarcq et al., 1985) starting from the year 1980 till May, 2002 were used in our study (Table 1). The image sizes varied from 928×942 to 1007×1003 . Yearly histogram of observing days is depicted in Figure 2b. The average number of images available per year over the study period for Meudon is ≈ 254 .

2.3 Kanzelhohe Dataset

Kanzelhohe Solar observatory (KSO) full-disc H $_{\alpha}$ images (Figure 1c) starting from the year 2000 till April, 2018 were used in this study (Table 1). KSO comes under Global H $_{\alpha}$ Network (Pötzi et al., 2013). These filtergrams were captured through two different CCDs before and after the year 2008. Because of that, the images are of size 2032×2032 (before 2008) and 2048×2048 (since mid January, 2008). Yearly histogram of observing days is depicted in Figure 2c. The average number of images available per year over the study duration for KSO is ≈ 260 .

¹http://bass2000.obspm.fr/data_guide.php

²<http://cesar.kso.ac.at/>

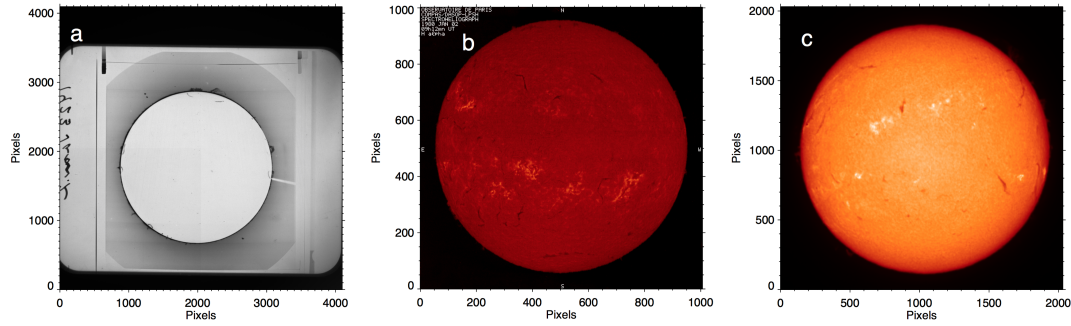


Figure 1. Raw datasets used for prominence detection. a) Representative raw KoSO Ca II K disc blocked spectroheliogram captured on January 02, 1923; b) Representative raw Meudon H α full disc spectroheliogram captured on January 02, 1980; c) Representative raw Kanzelhoehe H α full disc filtergram captured on January 21, 2003.

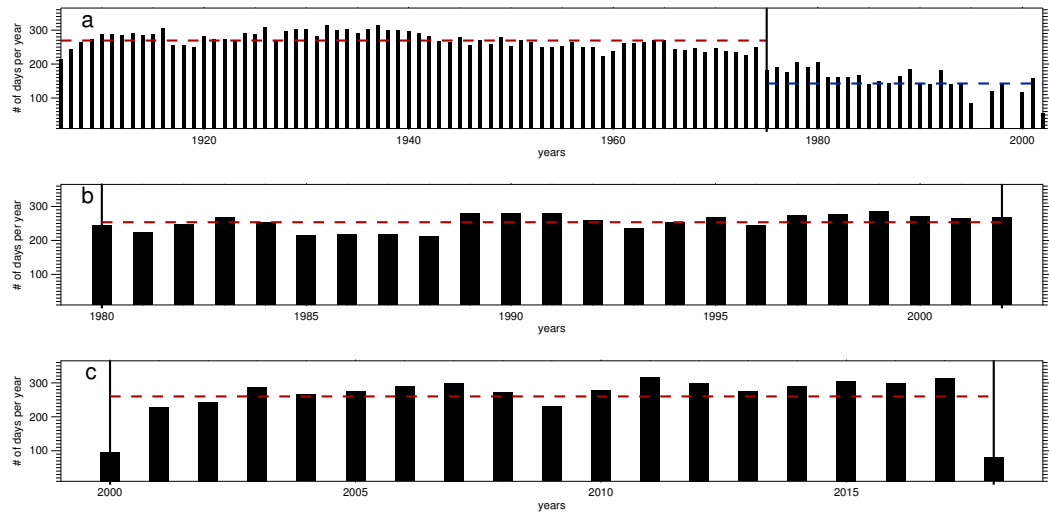


Figure 2. Histograms of observing days during the time period studied for KoSO, Meudon and KSO. a) Yearly histogram of available days in KoSO Ca II K disc blocked dataset. The red and blue dashed lines indicate the yearly mean before and after 1975 respectively; b) Yearly histogram of available days in Meudon H α full disc dataset. The red dashed line indicates the mean yearly observing days for entire study period; c) Yearly histogram of available days in KSO H α full disc dataset. The red dashed line indicates the mean yearly observing days for entire study period.

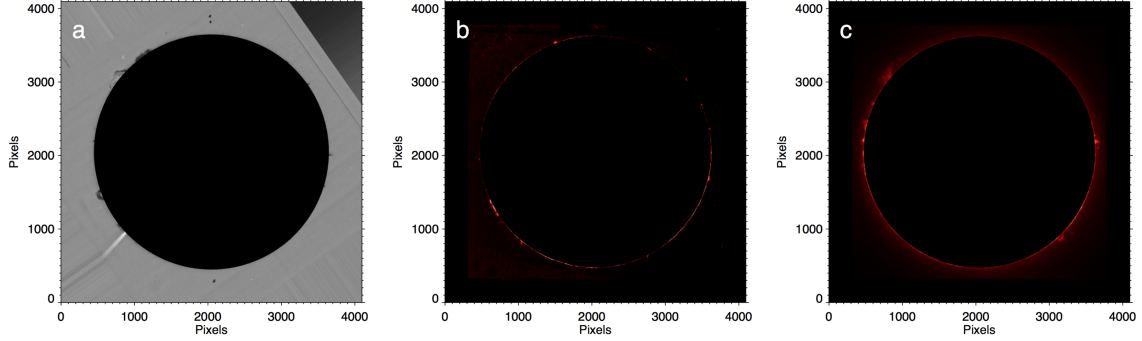


Figure 3. Calibrated disc-blocked images. a) Disc centered and radius normalised version of Figure 1a; b) Disc blocked, centered and radius normalised version of Figure 1b; c) Disc blocked, centered and radius normalised version of Figure 1c.

3 Analysis of Data

3.1 Calibration

Before detection of prominence locations, the digitised images had to go through few calibration steps. In the following two subsections we introduce the steps to calibrate both Kodaikanal Ca II K disc-blocked images and Meudon, Kanzelhoehe H α full-disc images in detail to make them ready for automated detection of prominence location using a single algorithm.

3.1.1 Calibration of Kodaikanal Ca II K disc-blocked images

All the digitized 4096×4096 raw images were initially binned to a size of 512×512 and ‘Prewitt’ (Sonka, Hlavac, & Boyle, 2014) edge detection operator was applied on the same to highlight the solar disc edge. Subsequently the edge detected image was thresholded to convert it to a binary form. The resulting binary image showed different edge features, prominent in the photographic film. To separate the disc out of all the features in the image, we used Circle Hough Transform (Chatterjee, Banerjee, & Ravindra, 2016; Sonka et al., 2014). For reducing the time and complexity we imparted a small search range about a nominal radius. This nominal radius value in pixel was obtained by dividing the disc angular size in arcsec, varying over a year, with the image pixel scale in arcsec. Subsequently, we acquired values of disc center coordinates and its radius.

To find the large scale intensity variation outside the solar disc, resized 512×512 images were blurred using 2D median filter of size 15×15 pixels. This filter size was a trade-off between prominence dimension and edge effect. The filtered image was subsequently resized to original size of 4096×4096 . This method has been commonly used to estimate asymmetric center-to-limb variation of intensity in full disc solar Ca II K images (Bertello, Ulrich, & Boyden, 2010; Chatterjee et al., 2016). The raw image was thereafter divided with the median filtered image to generate a normalized image.

It should be noted that just median filtering is not an accurate method for background normalization when the objective is to make the data ready for irradiance study (Chatzistergos et al., 2018) and may affect detection of features, measurement of contrast. We did not need the data to be photometrically calibrated as we opted for only detection of prominence locations avoiding measurement of individual feature areas.

Using the information obtained from Hough transform, we generated disc centered normalized images with a margin of 30% of the disc radii (r , in pixels) on both sides of solar disc to have provision of detecting large prominences. All the disc centered images of size $(2\lfloor 1.3r \rfloor + 1) \times (2\lfloor 1.3r \rfloor + 1)$ ($\lfloor \cdot \rfloor$ stands for the nearest integer function or the rounding operation) were converted

to images of size 4096×4096 . This step made disc radii constant throughout the study time. Because of the change of Sun-Earth distance over a year the radial extent of the images ($1.3r$ or 2048 pixels) varies between 1226 arcsec and 1265 arcsec. Also, in terms of image scale this variation is within $\approx 0.6 - 0.62$ arcsec/pixel. It can be seen from Figure 1a that the raw images have north-south pole marking denoted by double and single dots outside solar disc for north and south poles respectively. These dots were placed manually on the photographic plates/films considering p-angle astronomical ephemerides and rotation of images due to instrument over a day. They ensure alignment of images post digitization as small errors may occur while placing the plates inside digitizer unit. By detecting those dots we found the angle by which the image has to be rotated so that the North pole will be located right in upward direction. The region within a radius of 1600 pixels was removed to get rid of any effect due to any misalignment of blocking disc in the instrument and the actual solar disc. It is worth mentioning that the misalignment causes a stretch of solar limb to be connected to the actual prominences causing over-detection. A representative calibrated image from the raw image depicted in Figure 1a is shown in Figure 3a.

3.1.2 Calibration of Meudon and Kanzelhohe H_α images

Meudon Observatory images despite having N-S marks in vertical directions were not always aligned. Each of them were checked and aligned using p-angles from astronomical ephemerides as and when required. Full-disc images from Meudon and Kanzelhohe observatory (Figures 1b,c) were first smoothed using median filter and subsequently edge detection was performed to detect the disc edges. It is to be noted that apart from yearly variation of disc size, we dealt with different image sizes from both Meudon and Kanzelhohe for different periods of time. So, the size of the smoothing kernels was varied accordingly. On the binary image containing limb, Circle Hough transform was applied to find the disc center and radius. Using those information, disc centering was performed and the centered image was rotated for p-angle compensation. The disc portion of centered and rotation corrected image was then blocked using a circular mask. The disc-blocked image depicts the prominences (Figures 3b,c). Before applying the detection algorithm all these disc blocked images were brought to the size of 4096×4096 (same as Kodaikanal) keeping 30% margin outside limb.

3.2 Detection of Prominence locations

The calibrated images (I_{cal}), described in the last section, with image-center coordinates (c_x, c_y) were first converted to polar form (I_{polar}) using eq.(1).

$$I_{polar}(R, \theta) = \begin{cases} I_{cal}(\lfloor c_x + R \cos \theta \rfloor, \lfloor c_y + R \sin \theta \rfloor), & \text{if } \lfloor c_x + |R \cos \theta| \rfloor < 4096 \\ & \text{and } \lfloor c_y + |R \sin \theta| \rfloor < 4096 \\ 0, & \text{otherwise} \end{cases} \quad (1)$$

with $c_x = 2048$, $c_y = 2048$, $0 \leq R < \lfloor 2048\sqrt{2} \rfloor$ and $0^\circ \leq \theta < 360^\circ$. Rounding operation ($\lfloor \cdot \rfloor$) has been used to get integral pixel coordinates. Subsequently, polar images of size 2896 pixels \times 360 pixels (Figure 4) were produced from disc centered calibrated images of size 4096×4096 (Figure 3). For the polar maps pixel scale values obtained along R and θ are $\approx 0.6 - 0.62$ arcsec and 1° respectively.

The periodic curved patterns in the polar image I_{pol} stand for the four straight sides of I_{cal} and the regions above the curved portion are dark due to no data outside square I_{cal} . It can be seen that the curved edges in I_{pol} starts appearing for $R > 2048$ for obvious reasons. So, for segregating the prominences we considered I_{pol} pixels only for $1600 < R < 2000$. Within this region we calculated median (med_{pol}) and standard deviation (σ_{pol}) of pixel intensity. Thereafter we produced binary image (BW_{polar}) applying a threshold of $(\text{med}_{pol} - \sigma_{pol})$ to KoSO polar images making all the pixel intensity below that threshold as 1 and rest as 0. For Meudon and Kanzelhohe polar

images, binary version was produced by making all pixel intensities above ($\text{med}_{pol} + \sigma_{pol}$) as 1 and rest as 0. This difference was introduced considering whether prominence grey level is brighter or dimmer compared to background. Figure 4b depicts the binary image contours overlotted in red on the polar image shown in Figure 4a. This prominence segmented binary image presents itself with several problems. Firstly, it captures small scale intensity fluctuations in the background. Secondly, near the limb sudden jump of intensity occurs as a result of median filtering which connects the prominence structures making disjoint regions to appear as single connected region. Finally, the thresholding captures curved artefacts which are manifestations of scratches in the original images. As the background small scale non-uniformity in intensity has no relation with θ , count of thresholded pixels along R should follow the prominence height fluctuations. To partially get rid of background non-solar features, all the detected regions not connected to solar limb were removed. This step is demonstrated through Figures 4b,c. From the resulting binary image with reduced noise, we generated prominence radial pixel count curves as function of θ expressed by-

$$c(\theta) = \sum_R BW_{polar}(R, \theta)$$

$c(\theta)$ corresponding to Figure 4c is shown in Figure 4d.

It was obvious that local maxima of prominence heights are representatives of prominence locations. So, we calculated the locations of local maxima $\{\theta_M\}$ of $c(\theta)$. This process can be described as,

$$\{\theta_M\} = \arg_{0^\circ \leq \theta < 360^\circ} \left\{ \frac{dc(\theta)}{d\theta} = 0 \text{ and } \frac{d^2c(\theta)}{d\theta^2} < 0 \right\}$$

We refined these maxima locations by putting a threshold as function of mean (m) and standard deviation (σ) over $c(\theta_M)$. Finally we described the prominence locations as

$$\Theta = \theta_M(\arg_k \{c(\theta_M(k)) > m + 0.7\sigma\})$$

The coefficient of σ was selected by several iterations to select prominence locations efficiently. Count maxima at the locations Θ corresponding to Figure 4a are marked with red symbols on the count curve $c(\theta)$ in Figure 4b. Including the B_o angle correction, Θ was converted to prominence latitudes (L_{promin}) in the range $[-90^\circ, 90^\circ]$ using eq.(2).

$$L_{promin} = \sin^{-1}(\cos(B_o) \sin(\Theta)) \quad (2)$$

Along with the latitudes we also recorded the counts i.e. $c(\Theta)$. Figure 4c depicts the prominence locations with red symbols plotted above the prominences. It can be observed that the north and south pole markings did not get detected as prominences because they are detached from the limb.

From the detection of prominence locations, we obtained time latitude diagrams for prominences for Kodaikanal, Meudon and Kanzelhohe Observatory. Figure 5 depicts time-latitude distribution and fitted polar branches of prominences from 1906 till April, 2018. Time-latitude pattern of prominences detected using KoSO dataset is shown in Figure 5a. From this diagram we immediately notice the clear signature of pole-ward migration till the close vicinity of poles from cycle 15 through cycle 21 both in northern and southern hemispheres. Cycle 20 depicts two northern polar branches with the second being weaker than the first one. The nature of polar rush from cycle 15 until cycle 18 can be directly compared with the time-latitude plots depicted in Ananthakrishnan (1952); Ananthakrishnan (1954). Polar branch remains clear for northern hemisphere in cycle 22 whereas that in the southern hemisphere do not show clear trend. This is the effect of reduced number of observing days after cycle 21. The same algorithm applied on Meudon and Kanzelhohe H_α images manages to provide clear depiction of pole-ward migration from cycle 22 through cycle 24 (till mid of cycle 23 for Meudon in red and mid cycle 23 till cycle 24 for Kanzelhohe in Blue) in both hemispheres (Figure 5b). The combined dataset is presented with orange symbols in Figure 5c.

Figure 5d depicts the 13-month running average of monthly sunspot area variation in north and south from Greenwich dataset ³. Also, near minima there is consistent reduction in prominence counts at low latitudes for all the cycles. Cycle 23/24 minima shows a clear depiction of this and also that the prominences are created $\approx 55^\circ$ latitude (Figure 5b).

3.3 Polar Rush Fitting

Before fitting polar branches of prominence time-latitude diagram, we concatenated the three datasets namely KoSO, Meudon and Kanzelhoehe. Subsequently, 2-dimensional histogram of prominence time-latitude was generated using latitude bin of 1° and time bin of 0.1 years. Using the histogram density values the time-latitude plot was converted to an image. That image was thresholded to generate the binary version. For every latitudinal step, the mean temporal locations and standard error of the same were found for all the polar branches. It should be noted that we used each polar branch from one of the three observatories having major contribution in terms of data points. Now, most of earlier studies, calculated pole-ward migration rates through single linear fit. However, we clearly notice acceleration of polar rush in the time-latitude plot from our detection (Figures 5a,b). This has been reported earlier, indicating the change of polar rush close to pole (Makarov, Tlatov, & Sivaraman, 2001), though no concrete method of such estimation was presented. Fitting nonlinear functions such as higher order polynomials suffer from latitudinal dependence of error bars. To avoid this and also to quantify the change in migration rate with time (t), we opted for fitting with a piece-wise linear function defined by eq.(3).

$$t = \begin{cases} p_0^{(1)} + p_1^{(1)}\theta, & \text{if } 55^\circ \leq \theta < \theta_{sep} \text{ (Low Polar Zone)} \\ p_0^{(2)} + p_1^{(2)}\theta, & \text{if } \theta \geq \theta_{sep} \text{ (High Polar Zone)} \end{cases} \quad (3)$$

The separator latitude θ_{sep} was varied such that the fitting error is minimised. In this case two zones of pole-ward migration are created with rates $1/p_1^{(1)}, 1/p_1^{(2)}$. The rate uncertainties for those are given by $\Delta p_1^{(1)}/(p_1^{(1)})^2, \Delta p_1^{(2)}/(p_1^{(2)})^2$. Uncertainties in the coefficients denoted by $\Delta p_1^{(1)}, \Delta p_1^{(2)}$ were found by supplying the standard errors of mean temporal locations while fitting. Hereafter we use LPZ and HPZ as abbreviations for ‘Low Polar Zone’ and ‘High Polar Zone’ respectively.

Polar rush fits on the combined dataset using piece-wise linear function are marked by black lines in Figure 5c. As pointed out in several earlier studies (Ananthkrishnan, 1954; Bumba et al., 1990; Minarovjech et al., 1998a), after sunspot minimum prominence activity begins to develop in the high latitude zones between $40^\circ - 50^\circ$ latitudes and with the progress in sunspot activity, the prominence activity shifts towards pole with a rapid rush near sunspot maximum. Very similar phenomena can be noted from in the time-latitude plots (Figures 5a-d) when compared with epochs sunspot area cycle maxima (Figures 5e) for both the hemispheres. The mean of absolute differences between epoch of sunspot maxima and epoch of prominences reaching pole over all cycles comes about ≈ 1.5 years in north and ≈ 0.8 year in south from our detection.

The results on migration rates (units both in $^\circ/\text{year}$ and m/s) after applying piece-wise linear fit method are tabulated in Table 2 and Figures 6a, b. At LPZ the rates were seen to vary between $2.0 \pm 0.1 \text{ m/s}$ and $10.1 \pm 1.0 \text{ m/s}$ (rate values within brackets in Table 2 and right vertical axis in Figure 6a). Clear increase of migration rate was seen in HPZ on an average as the rates were seen to vary between $1.3 \pm 0.1 \text{ m/s}$ and $19.5 \pm 5.7 \text{ m/s}$ (Table 2 and Figure 6b). Cycle 19 was seen to dominate the migration rates in LPZ north and south. Also, rate in HPZ north was seen to be dominated by cycle 19. Because of higher error bars, same cannot be said for HPZ south. The average separator latitudes automatically found by the piece-wise linear fit came to be 67.5° and 69.2° for north and south respectively.

³<http://solarscience.msfc.nasa.gov/greenwch.shtml>

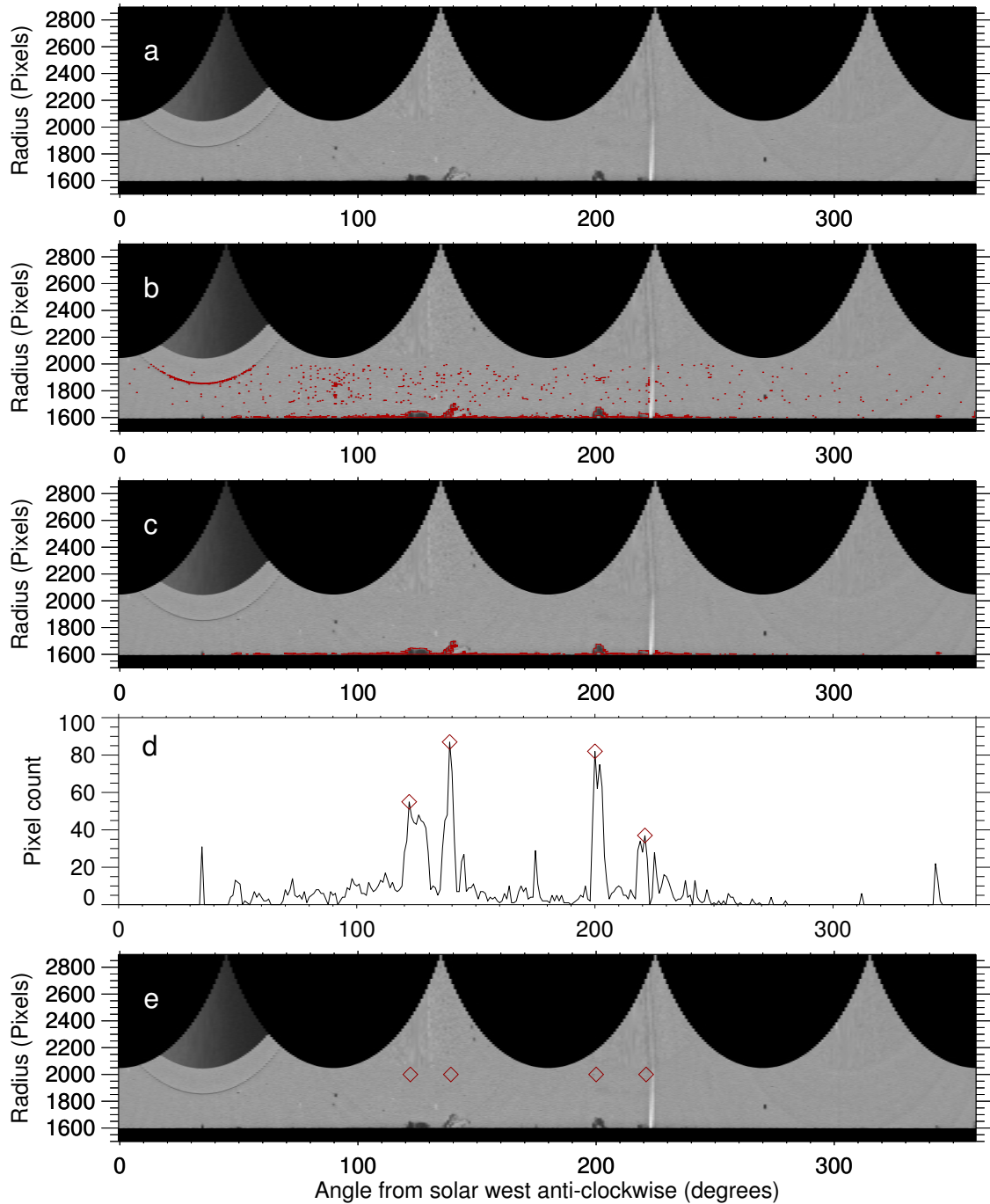


Figure 4. Steps for detection of prominence locations. a) Polar map generated from Figure 3a; b) Red contours correspond to the segmented regions after intensity thresholding of the polar map; c) Contours obtained after removing regions not connected to limb from (b); d) Counts of detected pixels along radius (c) for each angle w.r.t. solar west is plotted and local maxima with higher counts in red symbols are considered to be locations of prominence structures; e) Prominence locations identified in (d) over plotted on (a) with red symbols. As the solar disc does not contain any information here, a part of it near limb has been shown as black strip at the bottom of every panel.

Table 2. Pole-ward migration rates at different latitudes through piece-wise linear fit

Observatory	Cycle	rate in $^{\circ}$ /year (m/s)				separator latitude	
		LPZN	HPZN	LPZS	HPZS	N	S
Kodaikanal Ca II K	15	8.7 \pm 0.8 (3.4 \pm 0.3)	10.4 \pm 0.4 (4.0 \pm 0.2)	9.2 \pm 0.5 (3.6 \pm 0.2)	20.6 \pm 2.8 (7.9 \pm 1.1)	65 $^{\circ}$	71 $^{\circ}$
	16	5.6 \pm 0.5 (2.1 \pm 0.2)	19.3 \pm 1.5 (7.4 \pm 0.6)	8.1 \pm 0.4 (3.1 \pm 0.2)	50.6 \pm 14.8 (19.5 \pm 5.7)	63 $^{\circ}$	71 $^{\circ}$
	17	9.3 \pm 1.0 (3.6 \pm 0.4)	19.7 \pm 1.3 (7.6 \pm 0.5)	11.5 \pm 0.6 (4.4 \pm 0.2)	12.2 \pm 0.5 (4.7 \pm 0.2)	64 $^{\circ}$	70 $^{\circ}$
	18	10.8 \pm 0.8 (4.2 \pm 0.3)	19.6 \pm 3.2 (7.6 \pm 1.2)	11.0 \pm 1.0 (4.2 \pm 0.4)	23.6 \pm 2.6 (9.1 \pm 1.0)	70 $^{\circ}$	67 $^{\circ}$
	19	13.5 \pm 1.4 (5.2 \pm 0.5)	31.8 \pm 7.5 (12.3 \pm 2.9)	26.2 \pm 2.6 (10.1 \pm 1.0)	40.6 \pm 10.6 (15.6 \pm 4.1)	72 $^{\circ}$	71 $^{\circ}$
	20	9.6 \pm 0.6 (3.7 \pm 0.2)	3.4 \pm 0.2 (1.3 \pm 0.1)	7.5 \pm 0.5 (2.9 \pm 0.2)	14.1 \pm 2.2 (5.4 \pm 0.8)	71 $^{\circ}$	68 $^{\circ}$
	21	9.3 \pm 0.6 (3.6 \pm 0.2)	22.1 \pm 2.2 (8.5 \pm 0.8)	9.0 \pm 0.3 (3.4 \pm 0.1)	37.5 \pm 12.4 (14.4 \pm 4.8)	69 $^{\circ}$	74 $^{\circ}$
	22	11.3 \pm 0.6 (4.4 \pm 0.2)	21.4 \pm 2.4 (8.2 \pm 0.9)			69 $^{\circ}$	
	Meudon H $_{\alpha}$	22			5.6 \pm 0.2 (2.2 \pm 0.2)	16.6 \pm 1.5 (6.4 \pm 0.6)	
23		14.1 \pm 1.2 (5.4 \pm 0.5)	18.3 \pm 1.6 (7.0 \pm 0.6)	5.3 \pm 0.3 (2.0 \pm 0.1)	22.5 \pm 2.2 (8.7 \pm 0.9)	69 $^{\circ}$	65 $^{\circ}$
Kanzelhoehe H $_{\alpha}$	24	6.7 \pm 0.9 (2.6 \pm 0.3)	11.2 \pm 0.7 (4.3 \pm 0.3)	5.9 \pm 0.5 (2.3 \pm 0.3)	11.7 \pm 0.5 (4.5 \pm 0.2)	63 $^{\circ}$	64 $^{\circ}$

3.4 Correlation with Available Catalogues

To validate our prominence detection and understand the effect of using two different wavelengths on statistical basis, we compared our results with the available filament and prominence catalogues from Meudon H $_{\alpha}$ synoptic maps and LSO/KSO cross calibrated (Rybák et al., 2011) H $_{\alpha}$ series respectively (Figures 7a,b). To accomplish this, we first converted the butterfly diagram of our detection and also available catalogues to 2-dimensional histograms with temporal binning of 0.1 year and spatial binning of 1 $^{\circ}$ latitude. As our results primarily focus on polar-rush, we segregated the polar branches satisfying $|latitude| > 55^{\circ}$. For every cycle, we smoothed those polar branches with a kernel of dimension 1 year \times 10 $^{\circ}$ (Figures 8a-h). For every cycle, we correlated those smoothed histogram density images from our detection and the catalogues. The results of correlation for both north and south analysis are presented in Table 3. It can be observed that all the correlations vary within a range of $\approx 0.6 - 0.9$. It can be observed from the histogram images (Figures 8a-d) that for older cycles, where KSO data is not available, KoSO prominence data have an advantage over Meudon filament catalogue in depicting polar rush to higher latitudes with better data density and continuity. Poor data density in polar branch is also responsible for lower correlation coefficient. The visual match between our detection and LSO/KSO catalogue for cycle-24 (Figures 8e-h) is also reflected in correlation coefficients (>0.6) of Table 3.

4 Discussion

In this section we will first point out the relevance of our results with earlier results as recorded primarily from H $_{\alpha}$ observations. At KoSO prominences are recorded with Ca II K $_3$ line, representing a slightly lower height range in chromosphere as compared to H $_{\alpha}$. Thus one may expect the polar rush as calculated here may have some difference with other catalogues. However, through the comparison of Meudon H $_{\alpha}$ filament catalogue and our detected Ca II K prominences, a close match in polar branches for several cycles are observed. The signature of filament pole-ward migration in H $_{\alpha}$ is limited to $\approx 70^{\circ}$ latitudes as shown by Chatterjee, Hegde, Banerjee, and Ravindra (2017)

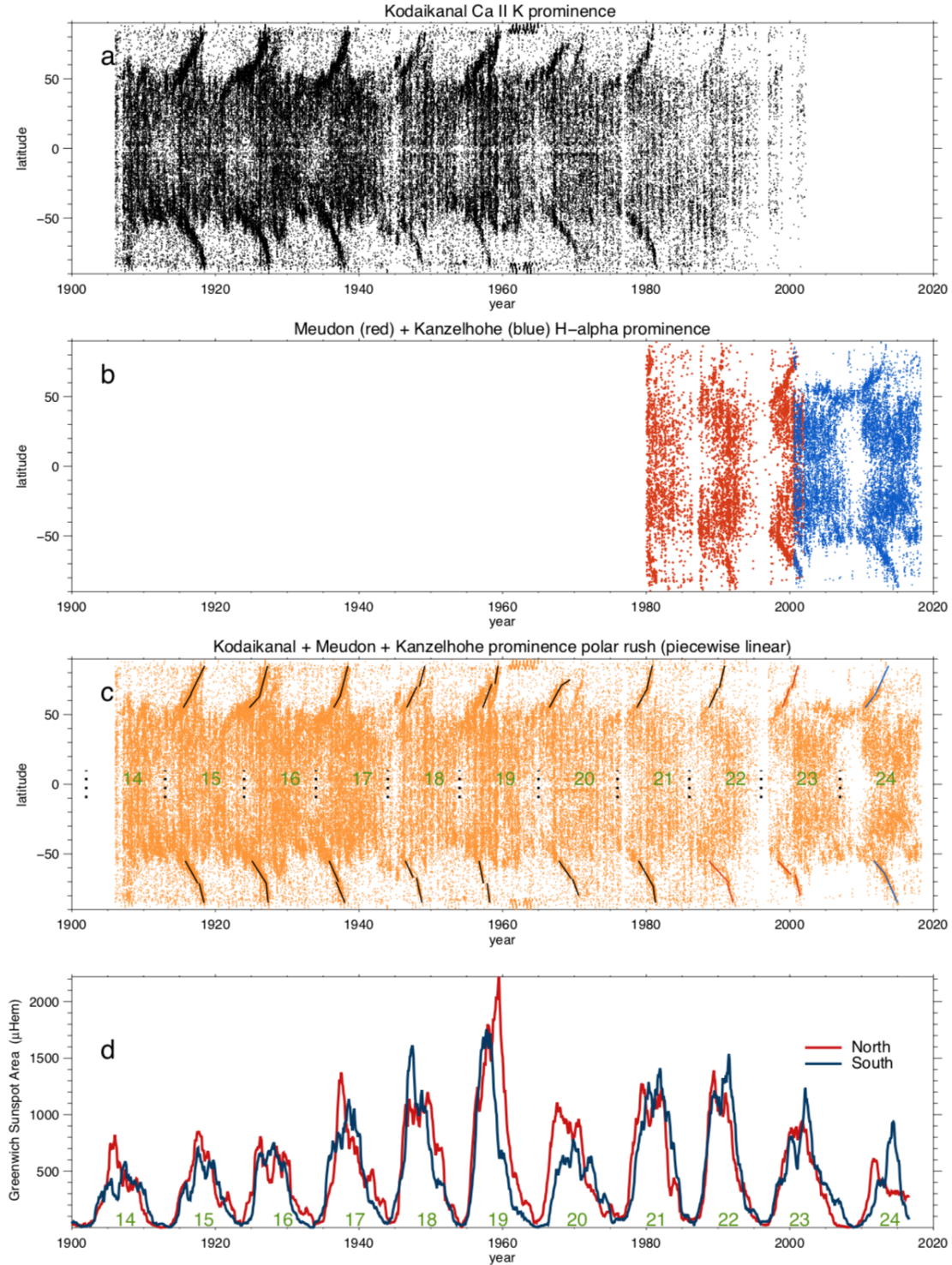


Figure 5. Prominence locations from 1906 until April, 2018. a) Time-latitude distribution of the KoSO prominences clearly depicting polar rush till latitudes close to 90° for cycles 15-21 in both northern and southern hemispheres; b) Detected prominence locations using same algorithm on Meudon and Kanzelhohe H_α data.; c) Piece-wise linear fits to the polar branches depicting the latitudes from which migration rate changes. Black, red and blue lines are generated respectively from KoSO, Meudon and Kanzelhohe data. Combined time-latitude distribution of prominences have been put in background with orange dots; d) 13-month running average smoothed Greenwich sunspot area cycle till 2016 for north and south.

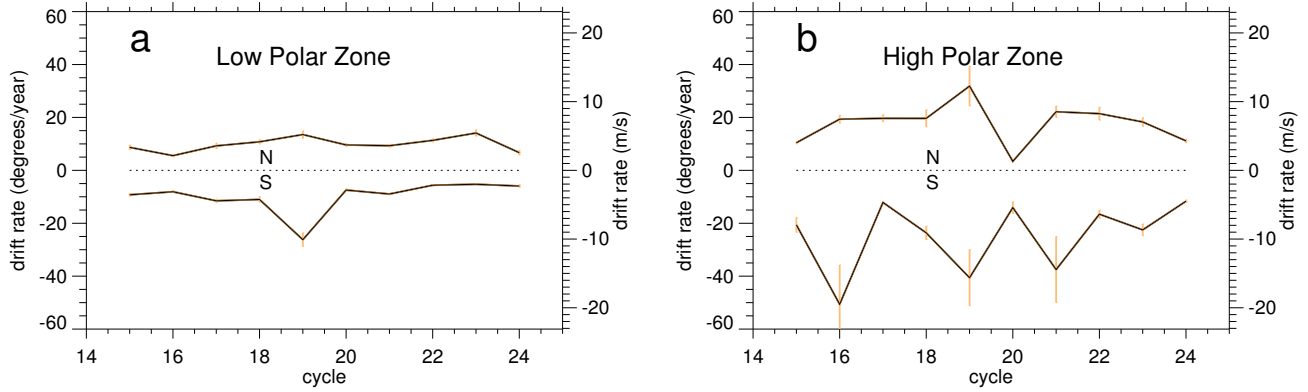


Figure 6. Cycle wise drift rate of polar prominences with error bars as vertical stretches in two latitude zones extracted from piece-wise linear fit. a) The variation of drift rates (degrees/year) with solar cycle number for both northern and southern hemispheres in latitude LPZ ranging from 55° to a separator latitude from which there is change in linear fit; b) the variation of drift rates (both in degrees/year and m/s) with solar cycle number for both northern and southern hemispheres in latitude HPZ ranging from separator latitude to $\approx 85^\circ$. It can be observed that the piece-wise linear fits successfully depicts cycle-to-cycle variation in drift rates along with north-south asymmetry taking in account the error bars. For both the latitude zones cycle 19 shows highest drift rate in northern hemisphere and it dominates south for latitude LPZ.

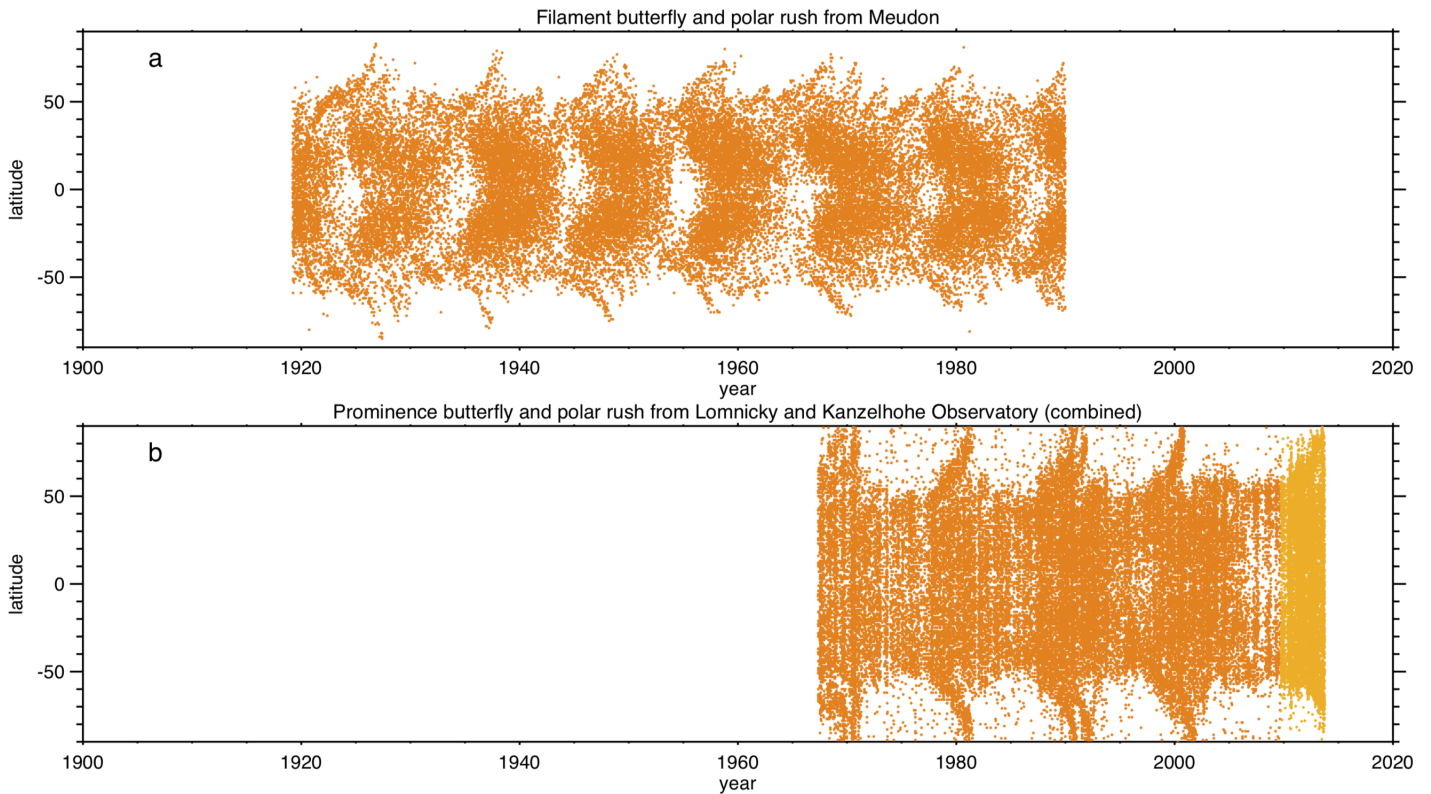


Figure 7. Available filament and prominence catalogues. a) Time-latitude distribution of on-disc filament centers from Meudon H α synoptic map catalogue; b) Time-latitude distribution of H α prominences from Lomnický (orange) and Kanzelhoehe (yellow) catalogue.

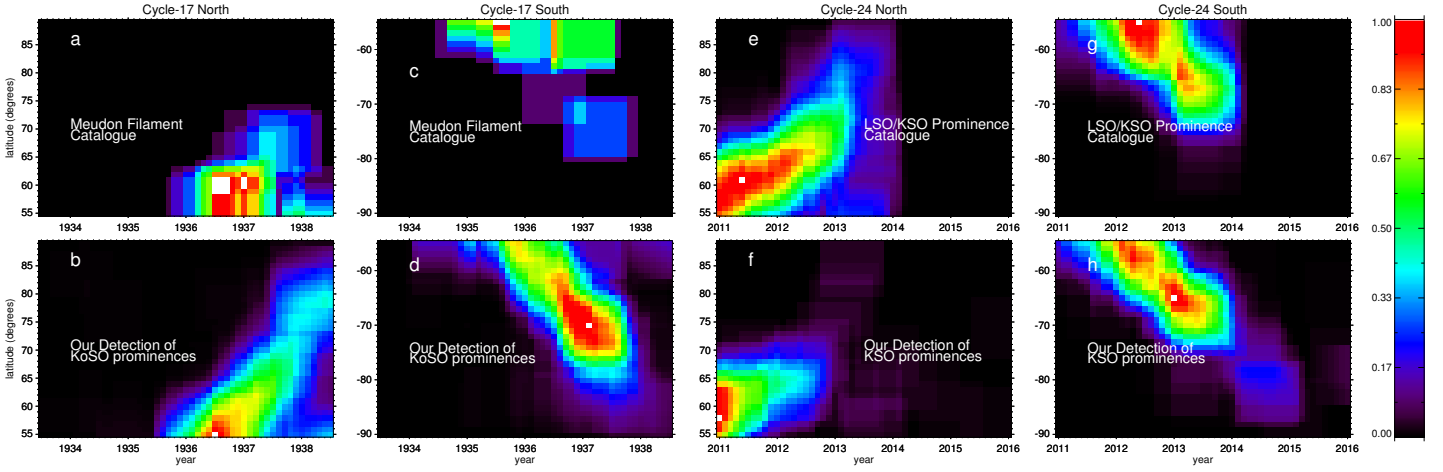


Figure 8. Comparison of polar rush between available catalogues and our detection. a) Density image of cycle-17 northern polar branch derived from Meudon filament catalogue; b) Density image of cycle-17 northern polar branch derived from our detection of KoSO prominences; c) Density image of cycle-17 southern polar branch derived from Meudon filament catalogue; d) Density image of cycle-17 southern polar branch derived from our detection of KoSO prominences; e) Density image of cycle-24 northern polar branch derived from LSO/KSO prominence catalogue; f) Density image of cycle-24 northern polar branch derived from our detection of KSO prominences; g) Density image of cycle-24 southern polar branch derived from LSO/KSO prominence catalogue; h) Density image of cycle-24 southern polar branch derived from our detection of KSO prominences. A colorbar has been provided on the right to compare the normalised prominence densities from different observatories.

Table 3. Correlation of polar branches from our detection and available catalogues

Cycle	Our detection vs Meudon catalogue		Our detection vs LSO/KSO catalogue	
	North	South	North	South
16	0.64	0.61	-	-
17	0.81	0.73	-	-
18	0.61	0.79	-	-
19	0.74	0.61	-	-
20	0.88	0.81	-	-
21	0.65	0.63	0.79	0.80
22	0.82	0.61	0.70	0.67
23	-	-	0.78	0.73
24	-	-	0.86	0.94

from KoSO data because of projection effect, poor contrast near limb and artifacts. This effect is also seen in the filament time-latitude distribution presented in Tlatov et al. (2016) and Mazumder et al. (2018). Thus the detected prominences served as better proxies to identify polar rush till close vicinity of poles. Clear correspondence between catalogue and detection from same data for overlapping cycles validated our detection technique. Information about prominences from KoSO Ca II K disc-blocked images in that sense acts as a complimentary dataset to the H_{α} filaments. It is also worth mentioning that in terms of time-latitude distribution of prominences, manual detection from the same prominence dataset of KoSO as reported in Ananthakrishnan (1952) shows close agreement with the automated detection as presented here. Because the Sun is mostly unipolar during maximum-to-minimum phase the locations detected during that phase may actually represent chromospheric jets near poles. However, such possibilities can only be decoupled through high cadence observations (Wang, 1999).

Though the fitting of polar branches has been done on combined dataset, each polar branch has major contribution from one of the three observatories. So, in the Table 2 each polar branch of a cycle has been listed against one among KoSO, Meudon and KSO. The separator latitudes while doing piece-wise linear fits gave an indication that migration rate of change occurs near about 70° latitude. The small error-bars also confirms that indeed drift rates keep on increasing towards poles.

Polar rush has important implication to meridional flow (Wang, Lean, & Sheeley, 2002) and turbulent diffusion (Petrovay et al., 2017). The computed polar migration rates as presented in this article, from the century-long prominence data may effectively constrain such parameters. For example, meridional flow for a solar cycle in the simulation by Wang et al. (2002) has been scaled according to the solar activity of the same cycle i.e. higher the activity more is the meridional flow rate. Makarov, Tlatov, and Sivaraman (2001) showed close correlation of integrated sunspot area in rising phase of a cycle having good correlation with pole-ward migration rate. This may further indicate that a correspondence between rate of polar rush and meridional circulation. However, there are certain discrepancies about latitudinal distribution of meridional flow rate near the poles and some studies predict it to be non-existent beyond 60° latitudes (Dikpati & Gilman, 2012). Thus, there can not be a single linear dependence between pole-ward migration rate and meridional flow rate. We want to point that polar rush can be caused by combination of diverse mechanisms such as surface diffusion/flux cancellation mimicking poleward migration of magnetic field and not just a passive advective transport.

As reported in Muñoz-Jaramillo et al. (2012), such study about proxy of polar field evolution is important as sunspot area combined with polar field evolution gives a complete picture of the long-term variation of solar hemispheric magnetic field. It has been shown before that polar faculae is a good proxy for polar magnetic field with 11 years average periodicity and also that the faculae count become maximum during solar minima (Sheeley, 2008).

So, the long-term data of prominences as presented here combined with historical polar faculae data can provide a better picture of polar magnetic activity in terms of reversal, build-up processes and may prove to be complementary to recent works on solar cycle predictions relying on long-term data-driven simulations (Bhowmik & Nandy, 2018).

5 Conclusions

In this paper, we first presented the calibration and processing of raw disc-blocked Ca II K dataset (1906 – 2002) from the Kodaikanal Solar Observatory. To improve the statistics of prominences we included the full disc H_{α} data from Meudon and Kanzelhoehe observatory till April, 2018 starting from 1980. Salient points of this work are listed below.

1. This study presented an unexplored series of disc-blocked Ca II K images for the first time.
2. Disc centered, rotation corrected images and subsequent polar maps of same size with constant disc radius were produced for the entire available dataset. Using the same automated algorithm, prominence locations were detected in all three datasets. To the best of our

- knowledge this is probably the first detailed result presented for century-long prominence observation for about 8 cycles from Kodaikanal and 3 cycles from Meudon and Kanzelhohe. All previous studies which contain long-term prominence detection from early 1900's either considered hand-drawn datasets (Tlatov et al., 2016) or semi-automated detection methods (Rybák et al., 2011).
3. Time-latitude distribution of detected prominences has been produced depicting a clear signature of polar rush for 10 cycles starting from 1906 till April, 2018 with initial ones mimicking those presented in Ananthakrishnan (1952) from same dataset. Cycle 20 was seen to have two northern polar branches with the second one being fainter and having higher migration rate. This is consistent with previous studies (Minarovjeh et al., 1998a; Waldmeier, 1973).
 4. Drift rates of polar prominences with latitude greater than 55° has been calculated with error bars through piece-wise fits (Table 2). Two zones (LPZ and HPZ) of polar-branch, found from the fits, clearly depicted change in migration rate with an increase from LPZ to HPZ for most of the cycles. This implies that the latitudes of polar prominences change non-linearly with time. The polar branches are seen well above 70° latitudes with nonzero migration rates whereas studies suggest meridional flow rate to vanish well before reaching poles (van Ballegoijen, Cartledge, & Priest, 1998; Dikpati & Gilman, 2012). Thus the implication of poleward migration rates on meridional flow needs to be well understood.
 5. Through piece-wise linear fits we found cycle to cycle variation of rates outside error bars for both the lower (LPZ) and higher (HPZ) latitude zones greater than 55° latitude. In LPZ, cycle 19 rate dominated others for both north and south. In HPZ only northern hemisphere was seen to be dominated by cycle 19.
 6. Correlation of polar branches with available filament/prominence catalogues depicted match with correlation >0.6 , validating our detection with an advantage of KoSO data dating back to the early part of last century.

However, this study is not devoid of limitations which we list below:

1. The datasets used in this study have not been cross-calibrated and thus the current images cannot be mixed to produce a single uniform disc-blocked dataset. That is the reason behind us presenting results from each observatory for non-overlapping periods.
2. We could not present the accuracy of the detection method or effect of the method on uncertainty in extracted results due to the lack of baseline detection method/manual annotations of prominences.

As a follow up work, we would like to address the above limitations and also combine KoSO H_α data series with this long-term off-limb Ca II K dataset to associate filament morphologies and prominences eruptions. Coronal green line (5303\AA) data (Minarovjeh, Rušin, & Saniga, 2007; Minarovjeh, Rybansky, & Rusin, 1998b; Petrovay et al., 2017; Sykora, 1985) and space based datasets will be useful sources to add to KoSO prominence dataset for bringing continuity. We hope that these newly calibrated data, as presented here for the first time will enhance the resources of long term archives.

Acknowledgments

We acknowledge all the observers at Kodaikanal over 100 years for their contribution to build this enormous resource. The Kodaikanal data archive is hosted at <http://kso.iiap.res.in>. We acknowledge the observers of Meudon and Lomnický-Kanzelhohe Observatory who made their data available through <http://bass2.obspm.fr/sitemap.php> and https://www.astro.sk/~choc/open/lso_kso_h-alpha_prominence_catalogue/lso_kso_h-alpha_prominence_catalogue.html respectively. We are grateful to the team members of the project on Reconstructing Solar and Heliospheric Magnetic Field Evolution Over the Past Century supported by the International Space Science Institute (ISSI), Bern, Switzerland for giving important suggestions to improve the manuscript. We would like to acknowledge the IUSSTF/JC-011/2016 project grant for

supporting this work. We also thank the Science & Engineering Research Board (SERB) for the project grant (EMR/2014/626).

References

- Abetti, G. (1957). *The sun*.
- Ananthakrishnan, R. (1952, July). Prominence Activity and the Sunspot Cycle. *Nature*, *170*, 156–158. doi: 10.1038/170156b0
- Ananthakrishnan, R. (1954, Aug 01). Prominence activity (1905–1952). *Proceedings of the Indian Academy of Sciences - Section A*, *40*(2), 72–90. Retrieved from <https://doi.org/10.1007/BF03048709> doi: 10.1007/BF03048709
- van Ballegooijen, A. A., Cartledge, N. P., & Priest, E. R. (1998, jul). Magnetic flux transport and the formation of filament channels on the sun. *The Astrophysical Journal*, *501*(2), 866–881. Retrieved from <https://doi.org/10.1086%2F305823> doi: 10.1086/305823
- Bertello, L., Ulrich, R. K., & Boyden, J. E. (2010, June). The Mount Wilson Ca ii K Plage Index Time Series. *Solar Physics*, *264*, 31–44. doi: 10.1007/s11207-010-9570-z
- Bhowmik, P., & Nandy, D. (2018, Dec). Prediction of the strength and timing of sunspot cycle 25 reveal decadal-scale space environmental conditions. *Nature Communications*, *9*, 5209. doi: 10.1038/s41467-018-07690-0
- Bogart, R. S., Hoeksema, J. T., & Scherrer, P. H. (1992, May). Measurement of the Polar Magnetic Fields at Wilcox Solar Observatory. In *American astronomical society meeting abstracts #180* (Vol. 24, p. 814).
- Bumba, V., Rusin, V., & Rybansky, M. (1990, July). Large-scale distribution of magnetic fields, green corona and prominences during an extended activity cycle. *Solar Physics*, *128*, 253–259. doi: 10.1007/BF00154161
- Chatterjee, S., Banerjee, D., & Ravindra, B. (2016, August). A Butterfly Diagram and Carrington Maps for Century-long CA II K Spectroheliograms from The Kodaikanal Observatory. *ApJ*, *827*, 87. doi: 10.3847/0004-637X/827/1/87
- Chatterjee, S., Hegde, M., Banerjee, D., & Ravindra, B. (2017). *ApJ*, *849*(1), 44. Retrieved from <http://stacks.iop.org/0004-637X/849/i=1/a=44>
- Chatterjee, S., Mandal, S., & Banerjee, D. (2017, June). Variation of Supergranule Parameters with Solar Cycles: Results from Century-long Kodaikanal Digitized Ca II K Data. *ApJ*, *841*, 70. doi: 10.3847/1538-4357/aa709d
- Chatzistergos, T., Ermolli, I., Solanki, S. K., & Krivova, N. A. (2018, Jan). Analysis of full disc Ca II K spectroheliograms. I. Photometric calibration and centre-to-limb variation compensation. *A&A*, *609*, A92. doi: 10.1051/0004-6361/201731511
- Chatzistergos, T., Ermolli, I., Krivova, N. A., & Solanki, S. K. (2019, May). Analysis of full disc Ca II K spectroheliograms. II. Towards an accurate assessment of long-term variations in plage areas. *A&A*, *625*, A69. doi: 10.1051/0004-6361/201834402
- Chatzistergos, T., Ermolli, I., Solanki, S. K., Krivova, N. A., Banerjee, D., Jha, B. K., & Chatterjee, S. (2019, Aug). Delving into the Historical Ca II K Archive from the Kodaikanal Observatory: the Potential of the Most Recent Digitised Series. *arXiv e-prints*, arXiv:1908.05493.
- D’Azambuja, L., & D’Azambuja, M. (1948). *Ann. Obs. Meudon*. *6*.
- Demarcq, J., Olivieri, G., Fruteau de Lacos, M., Marteau, M., Nicolas, M., & Roussel, R. (1985, December). A new instrument for solar observations. *L’Astronomie*, *99*, 557–566.
- Dikpati, M., & Gilman, P. A. (2012, jan). THEORY OF SOLAR MERIDIONAL CIRCULATION AT HIGH LATITUDES. *ApJ*, *746*(1), 65. Retrieved from <https://doi.org/10.1088%2F0004-637x%2F746%2F1%2F65> doi: 10.1088/0004-637x/746/1/65
- Engvold, O. (2015). Description and classification of prominences. In J.-C. Vial & O. Engvold (Eds.), *Solar prominences* (pp. 31–60). Cham: Springer International Publishing. Retrieved from https://doi.org/10.1007/978-3-319-10416-4_2 doi: 10.1007/978-3-319-10416-4_2
- Ermolli, I., Solanki, S. K., Tlatov, A. G., Krivova, N. A., Ulrich, R. K., & Singh, J. (2009, may). COMPARISON AMONG ca II k SPECTROHELIOGRAM TIME SERIES WITH AN AP-

- PLICATION TO SOLAR ACTIVITY STUDIES. *The Astrophysical Journal*, 698(2), 1000–1009. Retrieved from <https://doi.org/10.1088/0004-637x/698/2/1000> doi: 10.1088/0004-637x/698/2/1000
- Evershed, J. (1917, January). The Solar Prominence of 1916, May 26. *Kodaikanal Observatory Bulletins*, 3, 209.
- Evershed, J., & Evershed, M. (1917). *Mem. Kod. Observ.*, 1, 55.
- Fan, Y. (2015). Mhd equilibria and triggers for prominence eruption. In J.-C. Vial & O. Engvold (Eds.), *Solar prominences* (pp. 297–322). Cham: Springer International Publishing. Retrieved from https://doi.org/10.1007/978-3-319-10416-4_12 doi: 10.1007/978-3-319-10416-4_12
- Fleck, B., Hayashi, K., Rezaei, R., Vitas, N., Centeno, R., Cheung, M., ... Viticchie, B. (2012, May). On The Magnetic-Field Diagnostics Potential of SDO/HMI. In *American astronomical society meeting abstracts #220* (Vol. 220, p. 207.01).
- Gibson, S. E. (2018, Oct). Solar prominences: theory and models. Fleshing out the magnetic skeleton. *Living Reviews in Solar Physics*, 15(1), 7. doi: 10.1007/s41116-018-0016-2
- Gilbert, H. R., Holzer, T. E., Burkepile, J. T., & Hundhausen, A. J. (2000, July). Active and Eruptive Prominences and Their Relationship to Coronal Mass Ejections. *ApJ*, 537, 503-515. doi: 10.1086/309030
- Gopalswamy, N. (2015). The dynamics of eruptive prominences. In J.-C. Vial & O. Engvold (Eds.), *Solar prominences* (pp. 381–410). Cham: Springer International Publishing. Retrieved from https://doi.org/10.1007/978-3-319-10416-4_15 doi: 10.1007/978-3-319-10416-4_15
- Gopalswamy, N., Shimojo, M., Lu, W., Yashiro, S., Shibasaki, K., & Howard, R. A. (2003, March). Prominence Eruptions and Coronal Mass Ejection: A Statistical Study Using Microwave Observations. *ApJ*, 586, 562-578. doi: 10.1086/367614
- Harvey, J., & Munoz-Jaramillo, A. (2015, April). Vitalizing four solar cycles of Kitt Peak synoptic magnetograms. In *Aas/agu triennial earth-sun summit* (Vol. 1, p. 111.02).
- Hoeksema, J. T., Bush, R. I., Scherrer, P. H., Heck, C., Hurlburt, N., Shine, R., ... Title, A. (1997, May). Continuous Observations of Solar Magnetic Fields from SOI/MDI on SOHO. In *Aas/solar physics division meeting #28* (Vol. 29, p. 884).
- Joshi, N. C., Bankoti, N. S., Pande, S., Pande, B., & Pandey, K. (2009, December). Study of Distribution and Asymmetry of Solar Active Prominences during Solar Cycle 23. *Solar Physics*, 260, 451-463. doi: 10.1007/s11207-009-9446-2
- Liu, K., Wang, Y., Shen, C., & Wang, S. (2012, January). Critical Height for the Destabilization of Solar Prominences: Statistical Results from STEREO Observations. *ApJ*, 744, 168. doi: 10.1088/0004-637X/744/2/168
- Livingston, W., & Harvey, J. (1971). The Kitt Peak Magnetograph. Iv: 40-CHANNEL Probe and the Detection of Weak Photospheric Fields. In R. Howard (Ed.), *Solar magnetic fields* (Vol. 43, p. 51).
- Lockyer, W. J. S. (1908, June). Prominence and Coronal Structure. *Nature*, 78, 174-175. doi: 10.1038/078174c0
- Lockyer, W. J. S. (1922, April). On the relationship between solar prominences and the corona. *MNRAS*, 82, 323. doi: 10.1093/mnras/82.6.323
- Lockyer, W. J. S. (1931, May). On the relationship between solar prominences and the forms of the corona. *MNRAS*, 91, 797. doi: 10.1093/mnras/91.7.797
- Lugaz, N. (2015). Eruptive prominences and their impact on the earth and our life. In J.-C. Vial & O. Engvold (Eds.), *Solar prominences* (pp. 433–453). Cham: Springer International Publishing. Retrieved from https://doi.org/10.1007/978-3-319-10416-4_17 doi: 10.1007/978-3-319-10416-4_17
- Mackay, D. H. (2015). Formation and large-scale patterns of filament channels and filaments. In J.-C. Vial & O. Engvold (Eds.), *Solar prominences* (pp. 355–380). Cham: Springer International Publishing. Retrieved from https://doi.org/10.1007/978-3-319-10416-4_14 doi: 10.1007/978-3-319-10416-4_14

- Makarov, V. I., Tlatov, A. G., Callebaut, D. K., Obridko, V. N., & Shelting, B. D. (2001, February). Large-Scale Magnetic Field and Sunspot Cycles. *Solar Physics*, *198*, 409-421. doi: 10.1023/A:1005249531228
- Makarov, V. I., Tlatov, A. G., & Sivaraman, K. R. (2001, August). Does the Poleward Migration Rate of the Magnetic Fields Depend on the Strength of the Solar Cycle? *Solar Physics*, *202*, 11-26. doi: 10.1023/A:1011855103278
- Makarov, V. I., Tlatov, A. G., & Sivaraman, K. R. (2003, May). Duration of Polar Activity Cycles and Their Relation to Sunspot Activity. *Solar Physics*, *214*, 41-54. doi: 10.1023/A:1024003708284
- Martens, P. C., & Zwaan, C. (2001, Sep). Origin and Evolution of Filament-Prominence Systems. *ApJ*, *558*(2), 872-887. doi: 10.1086/322279
- Martin, S. F. (2015). The magnetic field structure of prominences from direct and indirect observations. In J.-C. Vial & O. Engvold (Eds.), *Solar prominences* (pp. 205-235). Cham: Springer International Publishing. Retrieved from https://doi.org/10.1007/978-3-319-10416-4_9 doi: 10.1007/978-3-319-10416-4_9
- Mazumder, R., Bhowmik, P., & Nandy, D. (2018, Nov). The Association of Filaments, Polarity Inversion Lines, and Coronal Hole Properties with the Sunspot Cycle: An Analysis of the McIntosh Database. *ApJ*, *868*(1), 52. doi: 10.3847/1538-4357/aae68a
- Minarovjeh, M., Rušin, V., & Saniga, M. (2007, April). Time-Latitudinal Dynamics of Magnetic Fields and the Green Corona Over Three Solar Cycles. *Solar Physics*, *241*, 263-268. doi: 10.1007/s11207-007-0239-1
- Minarovjeh, M., Rušin, V., & Saniga, M. (2011, October). Synoptic charts of solar magnetic fields. *Contributions of the Astronomical Observatory Skalnaté Pleso*, *41*, 106-112.
- Minarovjeh, M., Rybansky, M., & Rusin, V. (1998a). Prominences and the Green Corona Over the Solar Activity Cycle. *Solar Physics*, *177*, 357-364. doi: 10.1023/A:1004948832097
- Minarovjeh, M., Rybansky, M., & Rusin, V. (1998b). Time-Latitude Prominence and the Green Corona Distribution Over the Solar Activity Cycle. In D. F. Webb, B. Schmieder, & D. M. Rust (Eds.), *Iau colloq. 167: New perspectives on solar prominences* (Vol. 150, p. 484).
- Moss, W. (1946). *Sol. Phys. Observ.*, *3*, 119.
- Muñoz-Jaramillo, A., Sheeley, N. R., Zhang, J., & DeLuca, E. E. (2012, July). Calibrating 100 Years of Polar Faculae Measurements: Implications for the Evolution of the Heliospheric Magnetic Field. *ApJ*, *753*, 146. doi: 10.1088/0004-637X/753/2/146
- Parenti, S. (2014, March). Solar Prominences: Observations. *Living Reviews in Solar Physics*, *11*, 1. doi: 10.12942/lrsp-2014-1
- Petrovay, K., Nagy, M., Gerjk, T., & Juhsz, L. (2017). Precursors of an upcoming solar cycle at high latitudes from coronal green line data. *Journal of Atmospheric and Solar-Terrestrial Physics*, -. Retrieved from <https://www.sciencedirect.com/science/article/pii/S1364682617307009> doi: <https://doi.org/10.1016/j.jastp.2017.12.011>
- Pötzi, W., Temmer, M., Veronig, A., Hirtenfellner-Polanec, W., & Baumgartner, D. (2013, April). The Kanzelhöhe Observatory. In *Egu general assembly conference abstracts* (Vol. 15, p. EGU2013-1459).
- Priyal, M., Singh, J., Ravindra, B., Priya, T. G., & Amareswari, K. (2014, January). Long Term Variations in Chromospheric Features from Ca-K Images at Kodaikanal. *Solar Physics*, *289*, 137-152. doi: 10.1007/s11207-013-0315-7
- Rusin, V., Rybansky, M., Dermendjiev, V., & Stavrev, K. Y. (1994, August). Catalogue of solar prominences 1987 - 1993. *Contributions of the Astronomical Observatory Skalnaté Pleso Supplement*, *24*, 135-136.
- Rušin, V., Rybanský, M., Dermendjiev, V., & Stavrev, K. Y. (1988). Catalogue of solar prominences (1967 - 1986). *Contributions of the Astronomical Observatory Skalnaté Pleso*, *17*, 63-292.
- Rybák, J., Gömöry, P., Mačura, R., Kučera, A., Rušin, V., Pötzi, W., ... Temmer, M. (2011, October). The LSO/KSO H α prominence catalogue: cross-calibration of data. *Contributions of the Astronomical Observatory Skalnaté Pleso*, *41*, 133-136.

- Schrijver, C. J., Elmore, C., Kliem, B., Török, T., & Title, A. M. (2008, February). Observations and Modeling of the Early Acceleration Phase of Erupting Filaments Involved in Coronal Mass Ejections. *ApJ*, *674*, 586-595. doi: 10.1086/524294
- Secchi, P. A. (1872, March). The solar prominences. *MNRAS*, *32*, 226. doi: 10.1093/mnras/32.5.226
- Sheeley, N. R., Jr. (2008, June). A Century of Polar Faculae Variations. *ApJ*, *680*, 1553-1559. doi: 10.1086/588251
- Shimojo, M. (2013, December). Unusual Migration of Prominence Activities in the Southern Hemisphere during Cycles 23-24. *PASJ*, *65*, S16. doi: 10.1093/pasj/65.sp1.S16
- Sonka, M., Hlavac, V., & Boyle, R. (2014). *Image processing, analysis, and machine vision*. Cengage Learning. Retrieved from <https://books.google.co.in/books?id=QePKAgAAQBAJ>
- Sykora, J. (1985, January). Time-Latitude Distribution of Green Corona Brightness during Solar Cycles 18 19 and 20. *Bulletin of the Astronomical Institutes of Czechoslovakia*, *36*, 61.
- Tandberg-Hanssen, E. (1974). Solar prominences. *Geophysics and Astrophysics Monographs*, *12*.
- Tandberg-Hanssen, E. (1998). The History of Solar Prominence Research (Review). In D. F. Webb, B. Schmieder, & D. M. Rust (Eds.), *Iau colloq. 167: New perspectives on solar prominences* (Vol. 150, p. 11).
- Tlatov, A. G., Kuzanyan, K. M., & Vasil'yeva, V. V. (2016, Apr). Tilt Angles of Solar Filaments over the Period of 1919 - 2014. *Solar Physics*, *291*(4), 1115-1127. doi: 10.1007/s11207-016-0880-7
- Verma, V. K. (2000, May). On the distribution and asymmetry of solar active prominences. *Solar Physics*, *194*, 87-101. doi: 10.1023/A:1005232619582
- Waldmeier, M. (1973, February). A Secondary Polar Zone of Solar Prominences. *Solar Physics*, *28*, 389-398. doi: 10.1007/BF00152309
- Wang, Y. M. (1999, Jul). *ApJL*, *520*(1), L71-L74 doi: 10.1086/312149
- Wang, Y.-M., Lean, J., & Sheeley, N. R., Jr. (2002, September). Role of a Variable Meridional Flow in the Secular Evolution of the Sun's Polar Fields and Open Flux. *ApJL*, *577*, L53-L57. doi: 10.1086/344196
- Wilcox Solar Observatory. (2000, November). In P. Murdin (Ed.), *Encyclopedia of astronomy and astrophysics*. doi: 10.1888/0333750888/4331
- Webb, D. F. (2015). Eruptive prominences and their association with coronal mass ejections. In J.-C. Vial & O. Engvold (Eds.), *Solar prominences* (pp. 411-432). Cham: Springer International Publishing. Retrieved from https://doi.org/10.1007/978-3-319-10416-4_16 doi: 10.1007/978-3-319-10416-4_16
- Yeates, A. R., & Mackay, D. H. (2009, Jan). Modelling the Global Solar Corona: III. Origin of the Hemispheric Pattern of Filaments. *Solar Physics*, *254*(1), 77-88. doi: 10.1007/s11207-008-9276-7
- Yeates, A. R., & Mackay, D. H. (2012, Jul). Chirality of High-latitude Filaments over Solar Cycle 23. *ApJL*, *753*(2), L34. doi: 10.1088/2041-8205/753/2/L34